

Algorithmic Considerations for Effective Global Search of Robust Low-Thrust Trajectories

Amlan Sinha ^{*} and Ryne Beeson [†]
Princeton, NJ, USA 08840

The growing interest in the cislunar domain over the past decade has led to an increasing demand for low-thrust missions to key orbits within this region. These low-thrust missions, typically characterized by long thrust arcs, are highly susceptible to operational disruptions such as unforeseen thruster outages or missed thrust events. Consequently, there is a critical need for efficient trajectory design frameworks which incorporate robustness against such anomalies. In this study, we utilize a robust trajectory design framework to explore the solution space for the Power and Propulsion Element (PPE) module to the Earth-Moon \mathcal{L}_2 Southern 9:2 Near Rectilinear Halo Orbit. We propose algorithmic enhancements to improve the global search for robust solutions, and present a comprehensive analysis of two approaches: a *nonconditional* approach which involves a purely random search for robust solutions versus a *conditional* approach which involves warm-starting the search for robust solutions using the non-robust solutions. Our results indicate that by using non-robust solutions as initial guesses for the robust solutions, it is possible to achieve significant improvements in both the rate of convergence and the robustness of the final solutions.

Nomenclature

J	=	objective function
f	=	natural dynamics
g	=	forcing dynamics
ξ	=	spacecraft state
u	=	spacecraft control
ω	=	random variable
N^\dagger	=	number of segments in the reference trajectory
N^ω	=	number of segments in the realization trajectory
τ_1	=	time where a missed thrust event begins

^{*}Ph.D. Candidate, Mechanical and Aerospace Engineering, Princeton University

[†]Assistant Professor, Department of Mechanical and Aerospace Engineering, Princeton University.

$\Delta\tau$ = duration of the missed thrust event

I. Introduction

As a part of their broader initiative to eventually reach Mars and expand human presence in the Solar System, NASA aims to establish the Lunar Orbital Platform-Gateway, a major milestone in the Artemis program. The Lunar Orbital Platform-Gateway, or simply the Lunar Gateway (LG), will serve as a pit stop for many future spacecrafts traveling to and from the lunar surface as well as those venturing beyond the Earth-Moon system, making it a vital cornerstone for ensuring sustainable human presence in the Solar System. The LG comprises a modular architecture with various elements or modules which shall launch separately and subsequently assemble in lunar orbits. Central to this study is the Power and Propulsion Element (PPE), a critical module of the LG. Equipped with a solar electric propulsion system, the PPE shall be responsible for providing necessary station-keeping and orbital transfer capabilities, and for eventually serving as a space tug for visiting spacecrafts. It is one of the most foundational components of the LG, and is scheduled to launch in conjunction with the Habitation and Logistics Outpost module in late 2025. Given the strict timelines of the overall program and the critical role of the PPE in ensuring the LG's operational readiness, its timely and successful deployment is of paramount importance. Its success is not only crucial for the Artemis program but also for the broader goals of establishing a sustainable human presence in cislunar space and beyond.

Low-thrust propulsion systems have been a key enabling technology for many missions in recent years, and sometimes are the only feasible choice for deep space missions, due to their characteristically high specific impulse, and therefore their ability to achieve higher effective mass ratio than their impulsive counterparts. However, designing low-thrust trajectories within complex multi-body gravitational environments, such as the cislunar space, presents significant challenges since such trajectories are highly sensitive to minor perturbations. Additionally, low-thrust propulsion systems have minimal control authority, and the thrust primarily acts to *gradually* perturb the spacecraft state toward minimizing an objective function. Given the limitations on the control authority, executing maneuvers precisely on schedule is crucial. However, certain anomalous events, such as impact with space debris, can cause the spacecraft to depart from its nominal operating conditions, and force it to enter a protective mode during which all thruster operations are switched off. If such an event coincides with a thrust arc, it results in what is known as a missed thrust event (MTE). MTEs are relatively common for low-thrust missions [1]. Unless accounted for during preliminary mission design, they can severely degrade the mission performance, and in some cases may even make the mission objective unachievable depending on available propellant mass, and remaining mission time.

The PPE is a vital component of the LG, and its timely delivery to its operational orbit is critical. The current baseline transfer for the PPE exhibits multiple long thrust arcs, one which lasts approximately 276 days [2]. By extrapolating the empirical probabilities of safe mode events from prior low-thrust mission data, we find a 33 % likelihood of encountering

one MTE during this thrust arc. An MTE can potentially result in significant deviations from the nominal trajectory, jeopardizing its ability to reach the target operational orbit, or result in significant increases in fuel consumption and/or flight time. The exigent timeline of the Artemis program, which affords minimal margin for error, warrants a more comprehensive understanding of the robust low-thrust solution space i.e., solutions that have been made resilient to MTEs.

A. Motivating Example

As a motivating example, consider a spacecraft on a low-thrust spiral trajectory around Earth, and our goal is to find a feasible minimum-fuel solution that connects this spiral to the Earth-Moon \mathcal{L}_2 Southern 9:2 Near Rectilinear Halo Orbit. Due to the extremely low thrust acceleration, solutions to this problem typically involve multiple revolutions with long thrust arcs, making them particularly vulnerable to MTEs. In the following discussion, we consider one such nominal spacecraft trajectory which consumes approximately 2,038 kg of fuel, and has a total time of flight of 225 days. To understand how an MTE would impact this solution, we consider an engine failure which prevents the spacecraft from executing the first thrust arc as it is aligning itself for the subsequent transfer. During the MTE, which lasts 2.5 days, the spacecraft drifts under the natural dynamics, and regains full thruster capability once the engines are back online. Our objective here is to find an alternate solution by reoptimizing the trajectory following the MTE subject to the same constraints as the nominal solution.

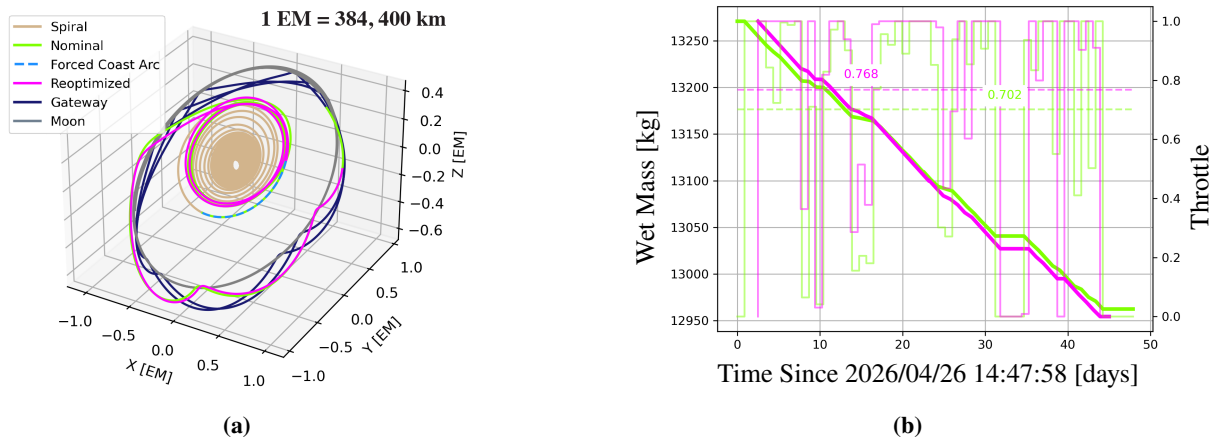


Fig. 1 In Fig. 1a, a nominal non-robust feasible trajectory is shown (green) along with the reoptimized trajectory (pink). A thruster outage lasting approximately 2.5 days prevents the spacecraft from executing the first burn, during which the spacecraft coasts under the natural dynamics (light blue). The reoptimized solution consumes ~ 8 kg more fuel than the nominal. In Fig. 1b, the corresponding wet mass and throttle profile for the post-spiral trajectory segment are shown for the nominal and the reoptimized solutions, with the average throttles shown as dashed lines. The low-thrust spiral phase is shown in beige, the moon’s trajectory in grey, and the NRHO in dark blue.

As shown in Fig. 1, the reoptimized trajectory deviates significantly from the nominal trajectory, initially trailing behind due to the forced coast arc. It quickly closes the gap, ultimately completing the mission slightly earlier than

the nominal. This, however, costs an additional 8 kg of fuel. The corresponding throttle profiles for the post-spiral phase reveal that while both solutions follow similar patterns, the reoptimized solution exhibits a higher average throttle in comparison to the nominal solution. It is important to note that although a viable solution was found in this case, such recovery may not always be possible. The spacecraft’s ability to recover from such engine failures depends on several factors, including its current state, the available on-board fuel, and the remaining mission time, underscoring the importance of robust trajectory design during the preliminary mission design phase. Doing so will allow us to not only build in the necessary margins, but also ensure that a robust alternative solution is readily available to deploy in the event that such outages disrupt the execution of a scheduled burn.

B. Survey Of Relevant Literature

The operational orbit chosen for the LG is the \mathcal{L}_2 Southern Near Rectilinear Halo Orbit with a 9:2 lunar synodic resonance [3–5]. For simplicity, we will simply refer to this orbit as the *NRHO* (i.e., in singular form) throughout the rest of the paper. The NRHO has an average perilune radius of 3,366 km, with a minimum altitude of 1,450 km over the northern lunar hemisphere. The apolune radius extends to about 70,000 km, with a minimum altitude of 68,000 km over the southern lunar hemisphere. The orbital period is approximately 6.56 days. It provides distinct advantages such as low orbit maintenance costs, convenient access to other key cislunar orbits as well as the lunar surface, and minimal eclipse durations. It is sufficiently stable, with an annual station-keeping Δv budget of approximately 15 mm/s [6]. These characteristics make it an ideal choice for LG’s operational orbit.

In recent years, there has been a growing interest from both academia and industry in better understanding the transfers to key cislunar orbits, with a particular focus on NRHO-bound transfers. Researchers have explored both impulsive [7, 8] and low-thrust [7, 9] transfers from (super) Geostationary Transfer Orbits to the NRHO. Ballistic transfer methods have also been investigated, providing alternative low-cost approaches for these missions [10–13]. Building on these studies, more recent research efforts have also explored eclipse-conscious transfers using higher-fidelity dynamical models [14, 15], as well as transfers leveraging the underlying dynamical structures [16]. The exploration of orbit maintenance and station-keeping strategies has become a critical research area [6, 17], underscoring the growing interest in long-term operations in the cislunar space. Beyond the initial exploration of transfers to the NRHO, research has also expanded to investigate impulsive and low-thrust trajectories for transitions between key cislunar orbits, including transfers between Northern and Southern NRHOs [18], between NRHOs and Distant Retrograde Orbits [19], and between NRHOs and other halo orbits [20, 21]. Considerable attention has also been devoted to lunar landing strategies [22] in both impulsive and low-thrust scenarios.

Despite recent advances, the robust solution landscape for low-thrust cislunar transfers remains relatively underexplored. Practical approaches to the missed thrust design problem, i.e., designing trajectories robust to MTEs, typically involve modifying a nominal trajectory under various missed thrust scenarios. These modifications may include

redesigning the nominal solution with lower duty cycles or with forced coast arcs at carefully selected points along the nominal trajectory. Based on changes in key performance metrics, empirical margin allocations are then made for the nominal solution, either in terms of additional fuel mass or flight time. For instance, the Dawn mission employed such an approach to ensure that the spacecraft could endure a minimum of twenty-eight days of shutdown time at any point along its nominal trajectory without significantly compromising its mission objectives [23, 24]. Similar techniques have been explored in various studies within the literature. For example, Laipert and Longuski examined the trade-offs between propellant and lateness margins when designing trajectories robust to MTEs [25]. Extending this work, Laipert and Imken used similar metrics to study the effects of multiple MTEs on a nominal trajectory, employing a Monte Carlo approach informed by historical missed thrust data from previous missions [26]. A recent study by Karn et al. attempts to uncover the effect of an MTE on the baseline transfer trajectory for the LG, but their focus is exclusively on the terminal insertion phase [27].

However, decoupling the trajectory optimization problem from maneuver execution uncertainties poses risks as such strategies can inadvertently shift sensitivity to different locations within the redesigned trajectory, and in many cases may produce solutions that are glaringly suboptimal compared to the nominal trajectory. State-of-the-art methods circumvent this issue by elevating the original optimal control problem to a higher-dimensional space [19, 28], enabling the simultaneous solution of a *reference* trajectory (the path we intend to fly) and multiple *realization* trajectories (the path we may be forced to fly after an MTE) from a-priori chosen points along the reference trajectory indicating where an MTE occurs. However, because the reference and realization trajectories are solved together within a single large optimization problem, the computational complexity may increase as the number of realizations increases. To address this, McCarty et al. [19] limit their analysis to a small number of realizations, while Venigalla et al. [28] propose an adaptive algorithm that adjusts the number of realizations to ensure that the minimum missed thrust recovery margin (i.e., the maximum amount of time a spacecraft may be allowed to coast while still being able to reach the terminal manifold once the thruster operations are resumed) remains above a certain threshold. However, both studies acknowledge that applying these methods to multibody gravitational models may pose additional challenges due to the chaotic nature of the underlying dynamics.

C. Contributions Of This Work

In this study, we present algorithmic techniques to improve the global search for robust low-thrust solutions in complex multibody dynamical environments. The main contributions of this study are summarized below:

- 1) We apply a robust trajectory design framework to a low-thrust cislunar transfer using a high-fidelity dynamical model, specifically to study robust low-thrust minimum fuel transfers for the PPE. We highlight the inherent complexities in designing low-thrust trajectories in the cislunar space, which becomes even more challenging in the presence of MTEs.

- 2) We demonstrate several algorithmic techniques which significantly enhances the global search for robust solutions. In particular, we compare two approaches for the global search of robust solutions: a nonconditional approach, which explores the solution space by randomly sampling the control solution from an a-priori chosen distribution, and a conditional approach, which leverages information from non-robust solutions to guide the optimizer toward robust solutions.
- 3) We provide a comprehensive statistical comparison between the non-robust solutions and the robust solutions using both global search approaches, offering insights into the trade-offs and benefits associated with each.

D. Organization Of This Paper

The paper is organized as follows. In §II.A, we present the robust trajectory design framework we utilize in this study, and in §II.B, we formulate the robust optimal control problem as a nonlinear program. In §III, we discuss the algorithmic techniques to enhance the global search for robust solutions. In particular, we discuss the two global search approaches for robust solutions, along with an adaptive segmentation strategy to promote congruity in control authority between the reference and realization solutions. We briefly discuss the dynamical model we use in this study in §IV, and then present the low-thrust transfer problem we apply our framework to in §V. In §VI, we statistically compare the robust solutions to the non-robust solutions found using both global search approaches. Finally, we highlight the importance of this work, discuss the limitations of the current approach, and provide an outlook on future efforts in §VII.

II. Problem Formulation

We first present the missed thrust design problem as it appears in this study, which can be shown to be a special case of the more general robust optimal control problem. For a deeper understanding of how the missed thrust design problem can be derived from the general robust optimal control problem, we direct the reader to the study by Sinha and Beeson [29]. For completeness, we restate the missed thrust design problem along with its formulation as a nonlinear program in the following sections.

A. Missed Thrust Design Problem

Let $(\Omega, \mathcal{F}, (\mathcal{F}_t)_{t \geq 0}, \mathbb{P})$ be a filtered probability space. Consider an optimal control problem where we aim to determine an extremal control solution $u^* \in \mathcal{U}$, with \mathcal{U} an admissible control set, to minimize the Bolza-type cost functional as follows:

$$\min_{u \in \mathcal{U}} \{J(u^\dagger) \equiv \phi(\xi_1^\dagger) + \int_0^1 \mathcal{L}(s, \xi_s^\dagger, u_s^\dagger) ds \mid \text{Eqs. (2), (3) are satisfied}\}, \quad (1)$$

where we consider the finite-time problem, and without loss of generality we normalize the time interval to be $[0, 1]$. ξ is the solution to a stochastic differential equation driven by the control $u \in \mathcal{U}$,

$$\begin{aligned} \text{s.t. } \xi_t^\omega = \xi_0^\dagger + \int_0^t f(s, \xi_s^\omega) ds + \int_0^{\tau_1(\omega) \wedge t} g(s, \xi_s^\omega, u_s^\dagger) ds \\ + \int_{\tau_2(\omega)}^t g(s, \xi_s^\omega, u_s^\omega) ds, \quad \forall t \in [0, 1], \forall \omega \in \Omega, \end{aligned} \quad (2)$$

taking values in a smooth manifold Ξ , satisfying the boundary conditions,

$$\xi_0^\omega \in \Xi_0, \xi_1^\omega \in \Xi_1, \quad \forall \omega \in \Omega, \quad (3)$$

In Eq. (2), the drift coefficient f represents the dynamics that are independent of the control, and the dispersion coefficient g encapsulates how the control input affects the dynamics. We assume that f contains no randomness, and that randomness in g occurs in a very specific way. In particular, we introduce random times that determine whether the dispersion coefficient (or forcing function) g , and consequently the control input u , affects the state dynamics ξ . The symbol \wedge is the minimum operator (i.e., $a \wedge b = \min(a, b)$).

We assume $\tau = \{\tau_1(\omega), \tau_2(\omega) \in (0, 1] \text{ s.t. } \tau_1(\omega) < \tau_2(\omega) \forall \omega \in \Omega\}$ to be a finite collection of random times with the random variable ω belonging to a random sample space identified by the unit circle i.e., $\Omega \simeq S^1 \simeq [0, 1]$, such that the uncertainty due to the random times τ specifies the initiation and duration of the MTE intervals. In particular, the initiation of an MTE occurs when $t = \tau_1$, and the duration of the MTE is given by $\Delta\tau(\omega) = \tau_2(\omega) - \tau_1(\omega) \forall \omega \in \Omega \in (0, 1]$. In what follows, we make the choice that $\tau_1(0) = \tau_1(1) > 1$, and hence the sample $\omega \in \{0, 1\}$ will correspond to a (deterministic) non-MTE trajectory for Eq. (2). We denote this special case, when $\omega \in \{0, 1\}$, with the \dagger symbol as u^\dagger and refer to the state solution ξ^\dagger as the *reference* solution. For all other cases, when $\omega \in (0, 1)$, we denote the control solution as u^ω and refer to the associated state solution ξ^ω as a *realization*.

The primary challenge in addressing the missed thrust design problem lies in defining and approximating the probability distribution for the random times τ , which is essential for meeting the dynamical constraints outlined in Eq. 2 that link the reference and realization solutions. Ideally, achieving a robust solution with formal guarantees would require accounting for the possibility of an MTE at every point along the nominal trajectory. Imken et al. [1] have analyzed previous low-thrust missions and suggested that the Weibull distribution is a suitable model for the initiation and duration times of an MTE. Because the Weibull distribution is continuous, achieving numerical tractability would require a sampling approximation. To keep the analysis tractable, however, we further simplify the robust trajectory design problem by making three critical assumptions about the random times τ :

- 1) Only one MTE will occur for any realization i.e.,
 - (i) For each $\omega \in \Omega$, assume that $|\tau(\omega)| \leq 2$.

- 2) Only a finite number of MTEs are allowed, with each corresponding to the start of a thrust segment,
 - (i) Assume that Ω is partitioned into a collection of N intervals $(E_i)_{i=1}^N$.
 - (ii) Assume that for every interval E_i , that we have for any $\omega_0, \omega_1 \in E_i$, the relation $\tau_1(\omega_0) = \tau_1(\omega_1)$.
- 3) Only a finite number of MTE durations are allowed.
 - (i) Assume that each interval E_i is further partitioned into a collection of M subintervals $(E_{i,j})_{j=1}^M$.
 - (ii) Assume that for every subinterval $E_{i,j}$, that we have for any $\omega_0, \omega_1 \in E_{i,j}$, the relation $\tau_2(\omega_0) = \tau_2(\omega_1)$.

B. Nonlinear Program

To solve the missed thrust design problem, we make use of Dynamically Leveraged Automated (N) Multibody Trajectory Optimization (DyLAN), a computational astrodynamics software package developed by Beeson et al. [30]. DyLAN brings together dynamical systems tools with local and global optimization methods to search for solutions of optimal control problems in multibody environments. We use a direct optimal control approach with forward-backward multiple shooting algorithm to convert the optimal control problem in Eq. (1) into a nonlinear program (NLP) [31]. The gradient-based numerical optimizer SNOPT [32] is then used to solve the NLP with initial guesses generated by the monotonic basin hopping global search algorithm [33–37]. We assume a finite-burn low-thrust (FBLT) model for the low-thrust trajectory. In the FBLT model, the trajectory is divided into discrete segments, and a continuous thrust is applied over the duration of each segment during which both the magnitude and the direction remain constant which approximates the change in velocity that would have been provided had the spacecraft's thruster been operated continuously at its maximum throttle setting for the full duration of the segment.

We define the NLP as follows:

$$\begin{aligned}
 & \min_{x^\dagger \in \mathbb{R}^{\bar{N}^\dagger}, x^\omega \in \mathbb{R}^{\bar{N}^\omega}} \{J(x^\dagger) = -m_f^\dagger\}, \\
 \text{subject to } & c_k^\dagger(x^\dagger) = 0, \quad c_k^\omega(x^\omega) = 0, \quad \forall k \in \mathcal{E}, \\
 & c_k^\dagger(x^\dagger) \leq 0, \quad c_k^\omega(x^\omega) \leq 0, \quad \forall k \in \mathcal{I},
 \end{aligned} \tag{4}$$

where the index set \mathcal{E} identifies the equality constraints, which consist of midpoint defect errors for the position, velocity, and mass continuity of the reference and realization. The index set \mathcal{I} identifies the inequality constraints, which consists of bounds on the control variables for the reference x^\dagger and realization x^ω (Table 2). The reference control decision variable has $\bar{N}^\dagger = 3N^\dagger + 4$ components given by,

$$x^\dagger = (T_s^\dagger, T_i^\dagger, T_f^\dagger, u_1^\dagger, u_2^\dagger, \dots, u_{N^\dagger}^\dagger, m_f^\dagger), \tag{5}$$

where T_s^\dagger is the shooting time, T_i^\dagger the initial coast time, T_f^\dagger the final coast time, and therefore the total time-of-flight is

$T_i^\dagger + T_s^\dagger + T_f^\dagger$. N^\dagger represents the number of finite burn thrust segments. $u_k^\dagger \in \mathbb{R}^3$ is a constant thrust vector for the k -th thrust segment that represents the throttle, in-plane, and out-of-plane thrust angle. The thrust segments each have equal time of T_s^\dagger/N^\dagger . Lastly, m_f^\dagger is the final delivered wet mass. A similar transcription follows for the non-robust control solution.

The transcription for the realization is similar, but x^ω will contain less control variables. The exact number is dependent on when the MTE for x^ω occurs. In particular, the total number of decision variables will be $\bar{N}^\omega = 3N^\omega + 4 = 3(N^\dagger - i) + 4$, where the MTE occurs at the start of the i -th thrust segment for the reference solution. More details about the transcription for the realization can be found in §III.A. The full control decision variable for the problem has $\bar{N}^\dagger + \bar{N}^\omega$ components given by,

$$x = (T_s^\dagger, T_i^\dagger, T_f^\dagger, u_1^\dagger, u_2^\dagger, \dots, u_{N^\dagger}^\dagger, m_f^\dagger, T_s^\omega, T_i^\omega, T_f^\omega, u_1^\omega, u_2^\omega, \dots, u_{N^\omega}^\omega, m_f^\omega)$$

A breakdown of the number of decision variables for both the non-robust and robust cases are summarized in Table 1.

Table 1 Number of Decision Variables (Number of Realizations = 1)

	Non-Robust	Robust
Number of Segments	N^\dagger	$N^\dagger + N^\omega$
Control Vector Components		
Time of Flight	3	6
Thrust Vector	$3N^\dagger$	$3(N^\dagger + N^\omega)$
Final Mass	1	2
Number of Constraints	7	14

III. Algorithmic Considerations for Efficient Robust Trajectory Design

A. Adaptive Segmentation

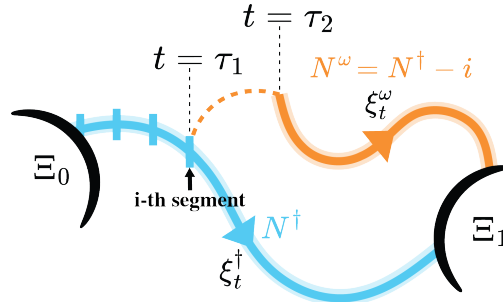


Fig. 2 A schematic demonstrating the adaptive segmentation strategy is shown here. An MTE occurs at the beginning of the i -th reference control segment, and as a result, the number of segments for the realization solution (orange) N^ω is adjusted such that $N^\omega = N^\dagger - i$ where N^\dagger denotes the number of segments for the reference solution (blue).

To promote congruence in control authority between the reference and realization solutions, an *adaptive segmentation* strategy is used to discretize the realization control solution. To illustrate, let us consider a reference solution divided into N^\dagger discrete control segments, with each thrust segment having equal time of T_s^\dagger/N^\dagger , and a realization solution which commences at the beginning of the i^{th} control segment within the reference control solution where $1 \leq i \leq N^\dagger$. The realization solution is similarly divided into N^ω discrete control segments, with each thrust segment having equal time of T_s^ω/N^ω . Since $T_s^\omega \leq T_s^\dagger$, if we naively assign $N^\omega = N^\dagger$, it would imply that each realization control segment now may span a shorter time interval since $T_s^\omega/N^\omega \leq T_s^\dagger/N^\dagger$ which would inadvertently result in a higher control authority for the realization solution in comparison to the reference solution. To avoid this incongruity in the control solution between the reference and the realization, we propose a segmentation for the realization which shifts N^ω by i such that $N^\omega = N^\dagger - i$ (Fig. 2). The adaptive segmentation strategy systematically adjusts the partitioning of control segments for each realization in alignment with its initiation point, thereby maintaining consistency in control authority between the reference and the realizations.

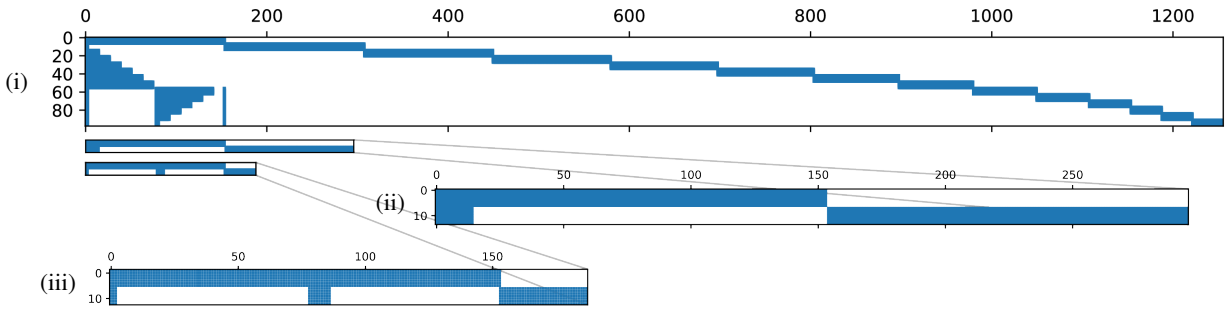


Fig. 3 Sparsity pattern of the Jacobian matrix for a low-thrust transfer with fifty segments is shown for three cases. Case (i): the reference solution is coupled with multiple realization solutions, Case (ii): the reference solution is coupled with a single realization solution initiating from the beginning of a reference control segment on the forward-shooting arc, and Case (iii): the reference solution is coupled with a single realization solution initiating from the beginning of a reference control segment on the backward-shooting arc.

Analytic derivatives are provided to the optimizer for both the non-robust and robust solutions, which significantly improves the efficiency of the design process. In preliminary analysis, we have seen that analytic derivatives significantly improve the convergence rates and the robustness of solutions in a simple cislunar transfer problem, especially when the reference solution is coupled with multiple realization solutions. The importance of analytic derivatives can be illustrated by visualizing the sparsity pattern of the Jacobian matrix, which represents the sensitivity of the midpoint defect errors with respect to the decision variables in the NLP. Fig. 3 illustrates the Jacobian sparsity pattern for three cases:

Case (i): The reference solution is coupled with multiple realization solutions,

Case (ii): The reference solution is coupled with a single realization solution initiating from the beginning of a reference control segment on the forward-shooting arc,

Case (iii): The reference solution is coupled with a single realization solution initiating from the beginning of a reference control segment on the backward-shooting arc.

As with case (i), if the reference trajectory is coupled with multiple realizations, the sparsity structure of the Jacobian matrix degrades significantly, exhibiting a drastic increase in the number of dense entries. The dense entries in the left subblock of the Jacobian matrix represent how the reference control segments prior to where the MTE begins influence the realization solutions. The higher degree of coupling introduces numerical sensitivity in the optimization process, and it may be more difficult to find robust solutions in that case. On the other hand, if the reference is only coupled with one realization, as with cases (ii) and (iii), and as considered in this study, there is a lesser degree of coupling in the Jacobian which makes it relatively easier to find robust solutions. Future work will provide more details on the improvement in performance between analytic derivatives and finite difference approximations [38].

B. Nonconditional (Random) Global Search

Table 2 Bounds on control variables for the reference solution x^\dagger and realization solution x^ω

	Reference					Realization				
	T_s^\dagger	T_i^\dagger	T_f^\dagger	u_k^\dagger	m_f^\dagger	T_s^\dagger	T_i^\dagger	T_f^\dagger	u_k^\dagger	m_f^\dagger
Lower Bound	0.0	0.0	0.0	$u_{k,\min}^\dagger$	0.0	0.0	0.0	0.0	$u_{k,\min}^\dagger$	0.0
Upper Bound	$T_{s,\max}^\dagger$	$T_{i,\max}^\dagger$	$T_{f,\max}^\dagger$	$u_{k,\max}^\dagger$	$m_{f,\max}^\dagger$	$(\frac{N^\dagger-i}{N^\dagger})T_{s,\max}^\dagger$	$T_{i,\max}^\dagger$	$T_{f,\max}^\dagger$	$u_{k,\max}^\dagger$	$m_{f,\max}^\dagger$

Two distinct methodologies can be adopted to conduct a global search for the robust solutions. One could utilize a random search method like the monotonic basin hopping (MBH) algorithm to search for the robust solutions, just as we do for the non-robust solutions. Initial guesses for $x = \{x^\dagger, x^\omega\}$ are sampled from a given random distribution, and a local gradient method is employed to refine the guess. As typical with such an approach, the decision variables are sampled from a bounded random distribution chosen a-priori by a mission designer (Table 2). In our implementation, we truncate the upper bound for T_s^ω by the ratio $(N^\dagger - i)/N^\dagger$, but leave the lower bound unchanged. We impose the same bounds on T_i^ω and T_f^ω as we do for T_i^\dagger and T_f^\dagger . The bounds for u_k^ω and m_f^ω are also the same as u_k^\dagger and m_f^\dagger . As typical of global search algorithms, without a suitable initial guess, the convergence times can likely be longer.

C. Conditional Global Search

The second approach draws from the assumption that robust solutions are likely to be *close* to the non-robust solutions, especially if $\Delta\tau$ is small enough. The non-robust solutions can then serve as an initial guess for the robust solution, enabling a local search in the vicinity of the non-robust solutions. In our implementation, we map the non-robust solution directly onto the reference solution to serve as initial guesses, but generating an effective initial guess for the realization solution cannot be done the same way because, in general, the number of control segments for the reference solution is not equal to the number of control segments for the realization solution. We modify the

bounds for the decision variables similarly to the nonconditional global search approach. But the initial guesses for the control variables play a crucial role in this approach since they define the local basin we will be searching using a gradient-based method. We set the initial guesses for $T_s^\omega = ((N^\dagger - i)/N^\dagger)T_s^\dagger$, $T_i^\omega = 0$, and $T_f^\omega = T_f^\dagger$. The control parameters associated with the non-robust control segments prior to where the MTE begins i.e., u_k^ω where $1 \leq k < i$, are discarded, and the others are used to inform the initial guesses for the remaining realization control segments i.e., $u_k^\omega = u_k^\dagger$ where $i \leq k \leq N^\dagger$.

IV. Dynamical Model

During the preliminary mission design phase, it can be beneficial to design cislunar trajectories using a high-fidelity dynamical model that more closely resembles the cislunar dynamics. This approach requires numerically solving differential equations which account for the gravitational influences of all relevant celestial bodies. Generally, the N-body dynamical model describes the motion of the spacecraft, P , within an inertial frame, \mathcal{I} , with respect to a central body, \oplus , under the gravitational effect of the same central body along with other perturbing bodies, Q_i , given by:

$$\mathcal{I} \ddot{q}_{P/\oplus} = -G(m_P + m_\oplus) \frac{q_{P/\oplus}}{|q_{P/\oplus}|^3} + G \sum_{i=0}^{N-1} m_{Q_i} \left(\frac{q_{P/Q_i}}{|q_{P/Q_i}|^3} - \frac{q_{\oplus/Q_i}}{|q_{\oplus/Q_i}|^3} \right) + \left\langle \frac{u}{m}, \hat{q}_{P/\oplus} \right\rangle \quad (6)$$

where q_{Q_j/Q_k} is the position of Q_j with respect to Q_k , m_{Q_i} is the mass of the body Q_i , u is the thrust vector, $\hat{q}_{P/\oplus}$ represents the coordinate direction in \mathcal{I} , and G represents the universal gravitational constant.

In this context, the mass m_\oplus represents the Earth; the mass m_P represents the PPE, and the additional masses m_{Q_i} correspond to other bodies that exert a non-negligible gravitational attraction, and m is the mass of the spacecraft. Since the spacecraft, at various points along its trajectory, makes close approaches to both the Earth and the Moon, both these celestial bodies are included in the N-body ephemeris model, along with the Sun and Jupiter since the solar and jovian gravitational effects significantly influence trajectories in the cislunar space. Although the higher-order terms in Earth's/Moon's gravity field can potentially impact the trajectory, for the sake of simplicity, the model was confined to contain only point-mass contributions from these bodies. The relative position of each perturbing body with respect to the central body q_{\oplus/Q_i} is computed instantaneously using ephemeris data available through the SPICE (Spacecraft, Planet, Instrument, C-matrix, and Events) database developed by the Navigation and Ancillary Information Facility at NASA [39].

For an LT trajectory, it is also necessary to account for the change in the spacecraft mass, which can be done by simply augmenting the mass to the state of the spacecraft, where the change in the mass m is governed by the differential equation:

$$\dot{m} = -\frac{|u|}{I_{sp}g} \quad (7)$$

where $|u|$ is the 2-norm and hence the thrust magnitude, $g = 9.806 \text{ m/s}^2$ is the gravitational acceleration on Earth and I_{sp} is the constant specific impulse of the propulsion system. We neglect other perturbations on the spacecraft e.g., solar radiation pressure, such that the only other term affecting the dynamics is the effect of the control input.

V. Problem Description

A. Orbital Parameters

Table 3 Geostationary Transfer Orbit

Parameter	Value
Period [days]	26.41
Mean Periapse Radius [km]	6,578
Mean Apoapse Radius [km]	40,278

Table 4 Reference \mathcal{L}_2 9:2 Southern NRHO

Parameter	Value
Period [days]	6.56
Mean Perilune Radius [km]	3,366
Mean Apolune Radius [km]	71,000

The baseline solution for the transfer of the PPE module, Design Reference Mission (DRM), has undergone several iterations. We pose our problem similar to the third iteration, DRM-3, which begins from the Geostationary Transfer Orbit and terminates at NRHO. The initial orbit is a 26.41 day orbit with a mean periapse radius of 6,578 km (periapse altitude of 207 km), and a mean apoapse radius of 40,278 km (apoapse altitude of 33,907 km) (Table 3), and the terminal orbit is a 6.56 day orbit with a mean perilune radius of 3,366 km (periapse altitude of 1,450 km) and a mean apolune radius of 71,000 km (periapse altitude of 68,000 km) (Table 4).

B. Spacecraft Parameters

Table 5 Spacecraft Parameters

Parameter	Value
Wet Mass [kg]	15,000
Dry Mass [kg]	5,000
Fuel Mass [kg]	10,000
Thrust Acceleration [m/s^2]	0.0002
Specific Impulse [s]	2,708

We assume the stack wet mass to be 15000 kg, with a dry mass equal to 5000 kg. The PPE will feature a combination of four Busek BHT-6000 thrusters and two NASA AEPS thrusters, yielding a total maximum thrust acceleration equal to 0.0002 m/s^2 , and a specific impulse equal to 2,708 s (Table 5).

C. Mission Design Phases

The DRM-3 comprises four distinct stages, each serving a critical role in the overall mission. The first is the *spiral phase*, during which the spacecraft thrusts continuously opposite to its instantaneous velocity vector, gradually

increasing its altitude through a low-thrust spiral trajectory. Following this is the *alignment phase*, where the thrust vector is chosen to achieve an optimal trajectory that minimizes fuel consumption, aligning the spacecraft for a transition to the next phase. The third is the *ballistic phase*, where the spacecraft coasts without thrust along a chosen ballistic coast arc toward its final destination. Finally, the mission enters the *insertion phase*, where a precise, small burn is executed to inject the spacecraft into its target orbit. In this study, we follow a similar approach for the spiral phase but we do not make any distinction between the alignment, ballistic, and insertion phases. Instead, we solve the problem in two phases: first, we solve the low-thrust spiral phase, and then, the terminal state from the *low-thrust spiral* phase acts as the initial condition for the subsequent *low-thrust transfer* phase which involves solving a minimum-fuel optimal control problem to the NRHO.

1. Low-Thrust Spiral

Our spiral phase, resembles closely that of DRM-3, differing only in its epoch and duration. Similar to DRM-3, the spiral phase involves simply applying a constant thrust anti-parallel to the instantaneous local velocity vector for a specific duration until the spacecraft is sufficiently far away from Earth. The initial epoch is chosen to be November 1, 2025, to keep the subsequent analysis consistent with the anticipatory launch date for the mission. In our simulations, the low-thrust spiral phase lasts ~ 176 days, taking the spacecraft to a distance approximately 28 Earth radii away. The duration was chosen such that the Jacobi integral of the spacecraft at the end of the spiral is sufficiently close to that of the NRHO. The spacecraft consumes approximately 1,729 kg of fuel during this phase. No MTEs were considered during this phase.

2. Low-Thrust Transfer

We then solve a minimum fuel optimal control problem, where the initial boundary condition corresponds to the terminal state at the end of the low-thrust spiral phase, and the terminal boundary condition is the NRHO. The optimizer is allowed to select the optimal insertion point on the NRHO, providing an additional degree of freedom to make necessary phasing corrections. In DyLAN, a binary space partitioning (bsp) file containing the ephemeris data for a target orbit can be supplied, which is then fit using spline interpolation. Using the interpolated data, the optimizer is able to compute the necessary gradients of the objective function with respect to the epoch, and therefore able to determine the optimal insertion point along the NRHO that minimizes the objective function. For the non-robust solutions, the maximum allowable initial coast time, final coast time, and shooting time are each set to 90 days, resulting in a maximum time of flight of 270 days for this phase. The trajectory is divided into 50 segments, which was seen to offer sufficient control authority, with the throttle profiles showing a characteristic bang-on-bang-off structure for the optimal trajectories. For the robust solutions, the same number of segments are used, and the bounds for the control parameters are adjusted as previously discussed in §III.

VI. Results and Discussion

In this section, we first discuss the robust solutions obtained via nonconditional global search in §III.B, and then the robust solutions obtained via conditional global search in §III.C. All simulations used in this study were performed using a 2.4 GHz Intel Broadwell processor with 96 cores.

A. Robust Solutions via Nonconditional Global Search

Table 6 Number of Solutions (Nonconditional Global Search)

	Non-Robust	Robust								
		$\Delta\tau$ [days]							τ_1	
		0.5	1.0	2.5	5.0	10.0	15.0	30.0	Forward	Backward
Number of Solutions	687	264	285	245	270	210	105	86	1275	190
Feasibility Ratio [%]	13.25	1.91	2.06	1.77	1.95	1.52	0.76	0.62	1.32	0.21
Optimality Ratio [%]	0.03	0.14	0.15	0.13	0.17	0.12	0.05	0.03	0.11	0.00

Using the nonconditional global search approach, a total of 687 solutions were found for the non-robust case, and 1,465 solutions for the robust case with varying τ_1 and $\Delta\tau$. The number of solutions, and their respective feasibility and optimality ratios, for each solution category are given in Table 6. For the robust solutions, the breakdown by τ_1 are categorized depending on whether τ_1 coincides with the forward shooting arc (denoted by ‘forward robust solutions’ from here onward), or the backward shooting arc (denoted by ‘backward robust solutions’ from here onward). The same sequence of random seeds is used for both non-robust and robust problems.

Naturally, the feasibility ratio for the non-robust case is significantly higher than the robust case. The optimality ratio for the non-robust case, however, is slightly lower. This is because the allowable total runtime for the non-robust simulations was much smaller than that of the robust simulations (18 hours for the non-robust case and 48 hours for each robust case). We hypothesize that the optimality ratio could be further improved by allocating a longer runtime for the non-robust case. The feasibility ratio for the robust solutions reveals an interesting trend as we vary $\Delta\tau$. When $\Delta\tau$ is sufficiently small (e.g., $\Delta\tau \leq 5$ days), the feasibility ratio remains relatively constant. If we continue increasing $\Delta\tau$ beyond this threshold, the feasible ratio starts to decrease. A similar pattern is observed in the optimality ratio as well. As we vary τ_1 , we notice that the forward robust case has a significantly higher feasibility ratio than the backward robust case. If the MTE occurs during the forward shooting arc, the spacecraft has more opportunity to correct its course, as it can simply stay on the same orbit until it can correct its phasing. However, if the MTE occurs during the backward shooting arc, the spacecraft can no longer do so since it may no longer be possible to correct the phasing through an extra revolution as it may violate the constraints on the allowable time of flight. The backward control segments correspond to regions around the Moon, where the dynamics can be significantly more sensitive, which poses additional challenges in obtaining feasible solutions for this case.

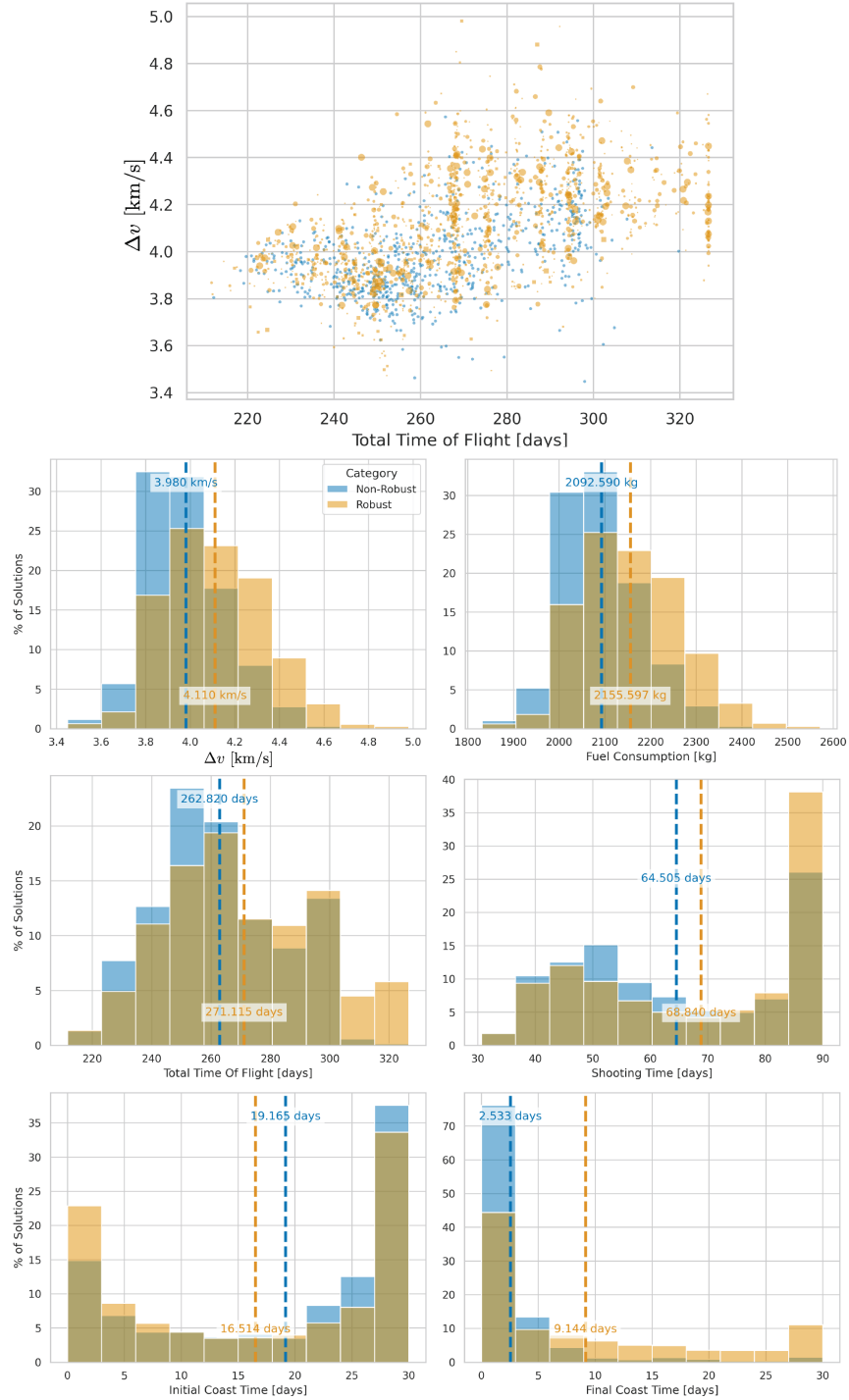


Fig. 4 Comparison of non-robust solutions with robust solutions obtained via unconditional global search. In the top figure, the forward robust solutions are denoted with a circle, and the backward robust solutions with a square. The size of the markers represents the value of $\Delta\tau$. The differences observed in the histograms for ‘ Δv ’ and ‘Fuel Consumption’ of the non-robust solutions are artifacts resulting from the different binning sizes in visualizing the histograms.

The family of robust solutions derived from the nonconditional approach is presented in Fig. 4. On average, these robust solutions exhibit higher fuel consumption than the non-robust solutions, and the distribution of fuel consumption appears wider. In extreme cases, some robust solutions can require approximately 200 kg more fuel compared to their non-robust counterparts. Moreover, the total time of flight for the robust solutions generally increases, with some solutions experiencing up to approximately 20 additional days compared to the non-robust solutions in the worst-case scenario. A breakdown of the time of flight into its constituent components shows that this increase is primarily driven by increases in the shooting and final coast times. In this case, the optimizer compensates for phasing errors by increasing both the shooting time and final coast time while simultaneously reducing the initial coast time. We hypothesize that the increase in final coast time for the robust solutions indicates that these solutions are being driven by the optimizer toward a stable invariant manifold earlier than their non-robust counterparts. Earlier alignment with the stable invariant manifolds enables the robust solutions to coast along the invariant manifold longer, potentially reducing the impact of MTEs.

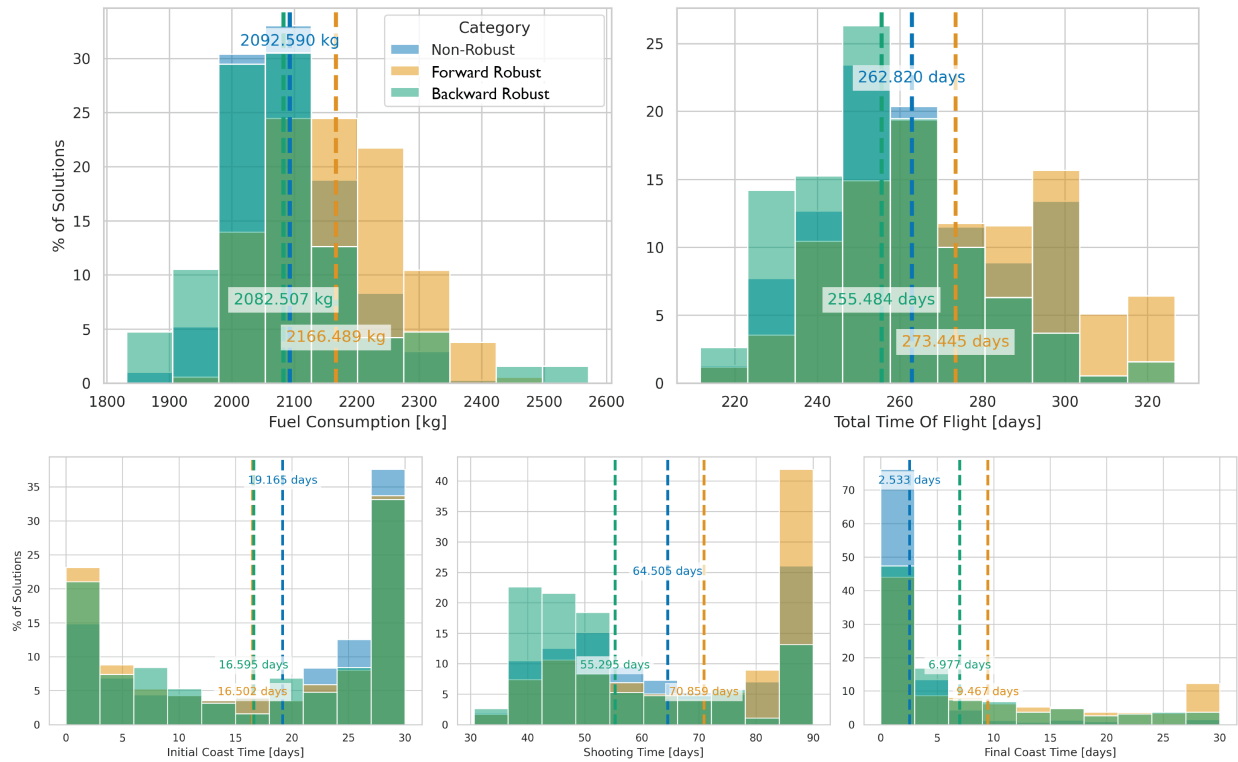


Fig. 5 Comparison of non-robust solutions with robust solutions via nonconditional global search categorized by τ_1

To understand how the robust solutions depend on τ_1 , we categorize the robust solutions depending on whether τ_1 coincides with a segment on the forward shooting arc (forward robust solutions) or a segment on the backward shooting arc (backward robust solutions). Our observations indicate that the backward robust solutions have a slightly

lower average fuel consumption, while the forward robust solutions show higher average fuel consumption compared to the non-robust case (Fig. 5). Given that solutions tend to be more sensitive as they approach the Moon, we would have expected the backward robust solutions to have a higher fuel consumption than the forward robust solutions. However, the backward robust solutions that ultimately achieve feasibility may have already been situated along a stable manifold arc, which minimizes the impact of the MTE on the key performance metrics. Consequently, the average fuel consumption of these solutions remains comparable to that of the non-robust solutions. It is also important to note the ‘tails’ in the distributions, where we observe that there are some solutions in the backward robust solution category which can consume approximately 50 kilograms more fuel than the forward robust solution category in the worst case.

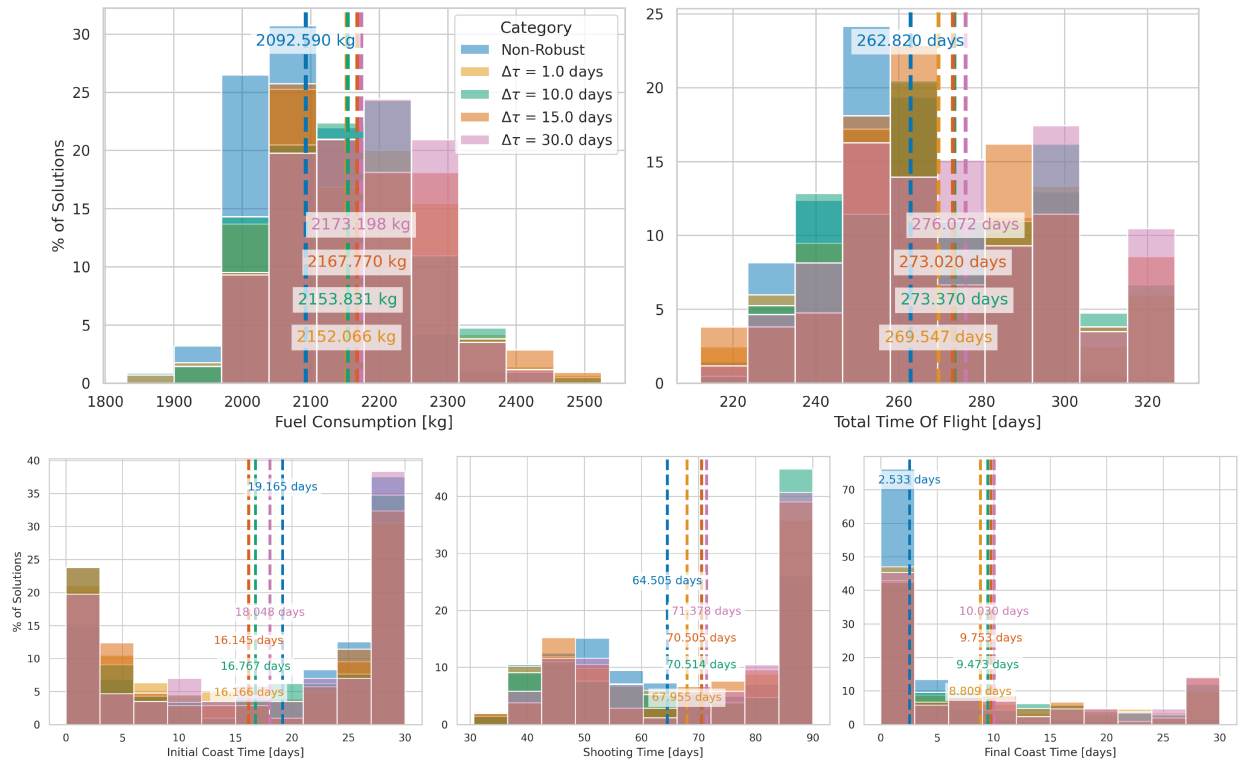


Fig. 6 Comparison of non-robust solutions with robust solutions via unconditional global search categorized by $\Delta\tau$

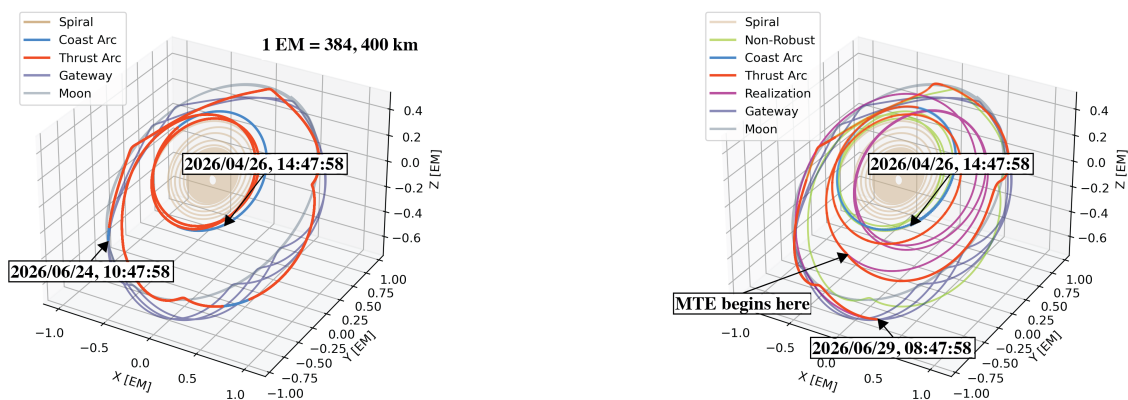
Next, to understand how the robust solutions depend on $\Delta\tau$, we categorize the robust solutions depending on $\Delta\tau$. Intuitively, as we continue to increase $\Delta\tau$, we would expect the spacecraft to maximize its throttle to correct the phasing disruption due to the MTE, which may result in an increase in the fuel consumption. As $\Delta\tau$ increases, we observe a monotonic increase in fuel consumption for the robust solutions, which aligns with our intuition (Fig. 6). Additionally, we notice a similar increase in both shooting time and final coast time days, accompanied by a decrease in initial coast time, which eventually increases the total time of flight. This behavior is consistent with the trends observed across the overall solution set.

B. Robust Solutions via Conditional Global Search

Table 7 Number of Solutions (Conditional Global Search)

	$\Delta\tau$ [days]							τ_1	
	0.5	1.0	2.5	5.0	10.0	15.0	30.0	Forward	Backward
Number of Solutions	217	198	244	172	157	151	107	829	417
Feasibility Ratio [%]	2.43	2.22	2.73	1.93	1.76	1.69	1.19	2.46	1.24
Optimality Ratio [%]	0.0006	0.0003	0.0006	0.0006	0.0009	0.0009	0.0000	0.0006	0.00

Using the conditional global search approach, a total of 1,246 robust solutions were identified. For each category of robust solutions, we use the entire set of feasible non-robust solutions as initial guesses. For instance, assuming τ_1 coincides with the beginning of control segments indexed by multiples of four, there are thirteen possible cases, yielding 8,931 initial guesses for each $\Delta\tau$. The breakdown of the number of solutions, along with the associated feasibility and optimality ratios, obtained through the conditional global search, is presented in Table 7. Notably, we observe that the feasibility ratios across the various categories are higher with the conditional global search compared to the nonconditional global search. Although the feasibility ratios decrease with increasing $\Delta\tau$, they remain higher than those obtained from the nonconditional global search. A similar trend is observed for τ_1 , where the backward robust solutions show a lower feasibility ratio than the forward robust solutions, but both are still higher than those from the nonconditional approach. However, the optimality ratio is significantly reduced, which makes sense, as by providing non-robust solutions as initial guesses, we effectively constrain the robust solutions to a basin where a locally optimal solution may not exist. This underscores the trade-offs with warm-starting the search for robust solutions with non-robust solutions.



(a) A non-robust solution is shown with the thrust arcs are shown in red, while the coast arcs are shown in blue.

(b) A robust solution ($\Delta\tau = 2.5$ days, $\tau_1 = 24$) is shown with the non-robust solution shown in green and realization in magenta. The corresponding thrust arcs for the robust solution is shown in red, and the coast arcs in blue.

Fig. 7 The low-thrust spiral phase is shown in beige, the moon's trajectory in grey, and the NRHO in dark blue.

A comparison between a non-robust and robust solution is shown in Fig. 7. A non-robust solution is shown in Fig. 7a. Warm-starting the robust solution search with this non-robust solution for the case where τ_1 coinciding with the beginning of the 24-segment and $\Delta\tau = 2.5$ days produces the robust solution shown in Fig. 7b. Both the reference trajectory and the realization trajectory are shown, where the realization trajectory corresponds to the trajectory we may fly if an MTE, lasting for 2.5 days, coincides with the beginning of the 24-th control segment in the reference solution. Initializing the robust solution with the non-robust solution leads to substantial deviations from the non-robust trajectory, resulting in a delay of five days for the insertion into the NRHO. Both the reference and the realization trajectories insert themselves at the same point on the NRHO, but each follow a significantly different trajectory.

Since we initialize the robust solutions using the non-robust solutions, we anticipate that the robust solutions will closely resemble the non-robust ones in terms of fuel consumption and time of flight. The results presented in Fig. 8 support this hypothesis, revealing a smaller gap in both fuel consumption and time of flight parameters between the non-robust and robust cases, when compared to the unconditional global search approach. By using non-robust solutions as initial guesses for the robust solutions, we achieve not only a reduction in average fuel consumption but also an improvement in the worst-case scenarios. The distribution of fuel consumption for the robust solutions becomes more comparable to that of the non-robust case, spanning approximately the same range for both Δv and total time of flight. This similarity is particularly evident when examining the solutions in the Δv versus total time of flight plane, where clusters of robust solutions closely align with those of the non-robust solutions. In contrast to the unconditional global search approach, we observe a decrease in the average total time of flight for the robust solutions as well. This is due to a decrease in the average shooting time and the average final coast time. Although there is a slight increase in the average initial coast time, the overall reduction in average total time of flight is primarily driven by the improvements in shooting time and final coast time.

Filtering the robust solutions by τ_1 , we once again observe a lower fuel consumption for the backward robust solutions, but a higher fuel consumption for the forward robust solutions in comparison to the non-robust solutions (Fig. 9). There also exists some backward solutions toward the tails of the distribution, which consume a significantly higher fuel than the forward solutions in the worst case. Interestingly, in this case, the time of flight for the robust solutions is similar for both forward and backward cases, and smaller than the non-robust. By performing this conditional global search, however, we are able to improve the average quality of solutions found in both categories compared to the unconditional global search, as evident by the smaller gap between the robust and the non-robust solutions in both categories.

Similar trends are observed for the solutions categorized by $\Delta\tau$ using the conditional global search approach, consistent with the findings from the unconditional global search (Fig. 10). Specifically, we see an increase in fuel consumption as $\Delta\tau$ increases. However, the gap between the non-robust and robust solutions in each category is narrower compared to what was seen in the unconditional global search approach.

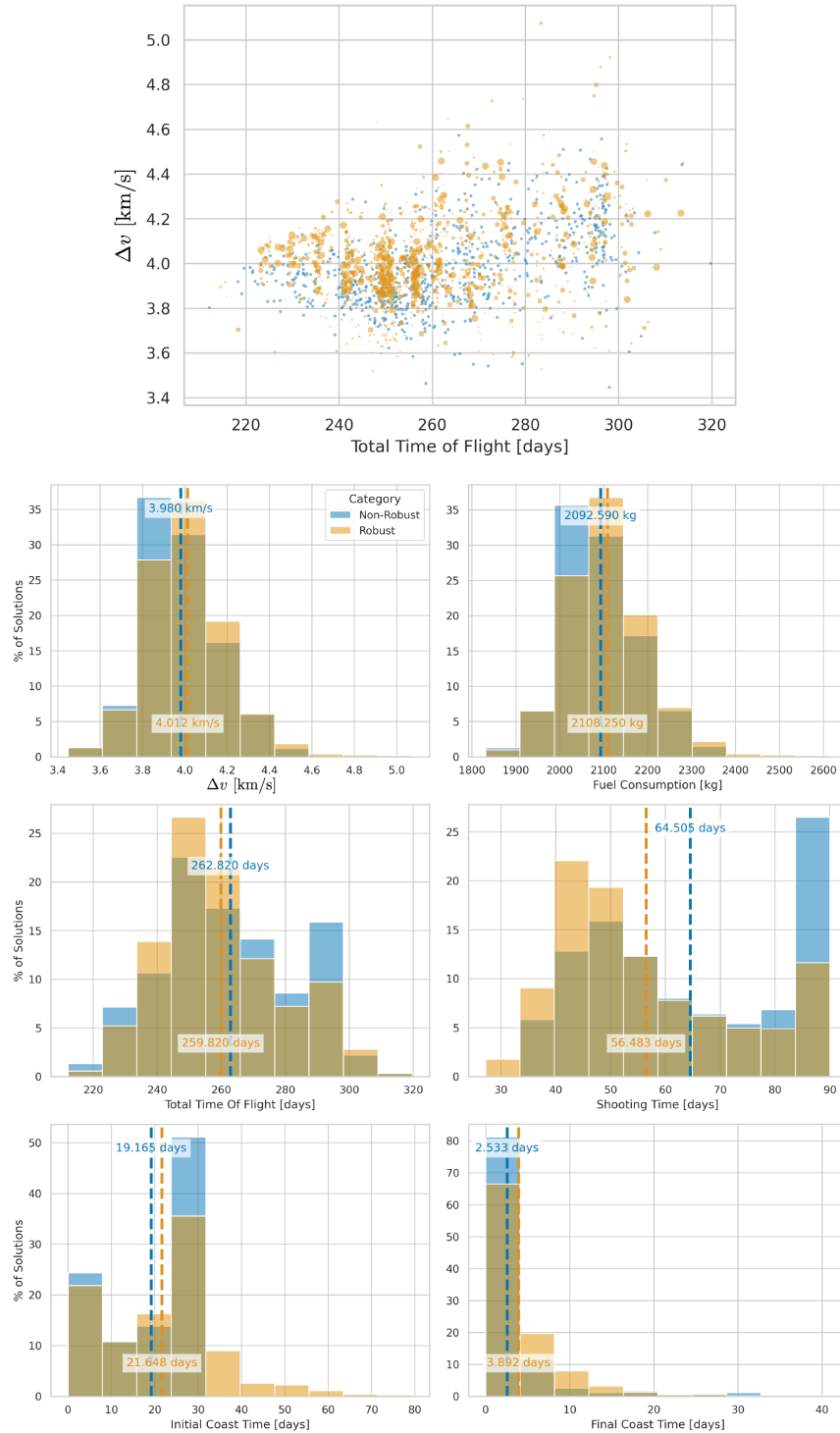


Fig. 8 Comparison of non-robust solutions with robust solutions obtained via conditional global search. In the top figure, the forward robust solutions are denoted with a circle, and the backward robust solutions with a square. The size of the markers represents the value of $\Delta\tau$.

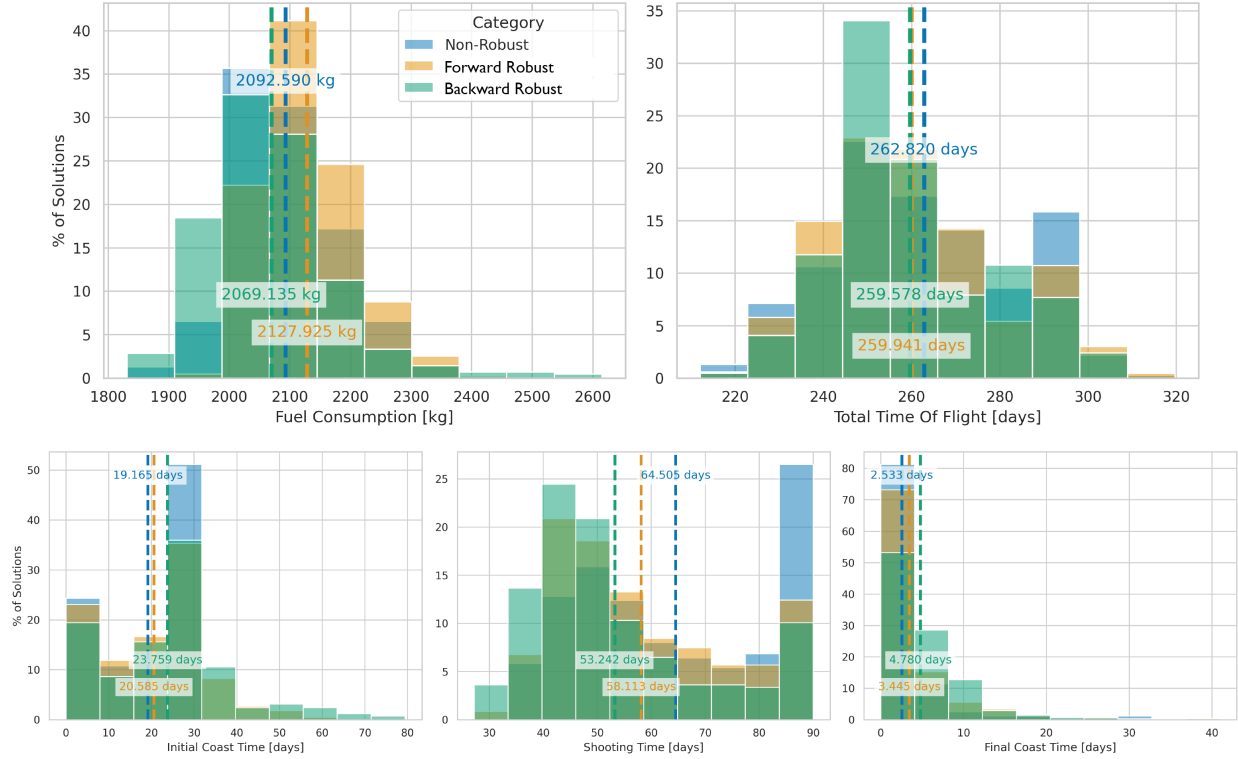


Fig. 9 Comparison of non-robust solutions with robust solutions via conditional global search categorized by τ_1

The advantages of employing a conditional global search approach are further illustrated in Fig. 11. We observe two key differences between the two approaches regarding average fuel consumption. First, using the global search approach, we fail to identify solutions for scenarios where τ_1 coincides with the last control segment irrespective of $\Delta\tau$ and where τ_1 coincides with the backward control segments with $\Delta\tau = 30$ days. In contrast, the conditional global search approach successfully yielded solutions in both these cases. Second, when initialized with non-robust solutions, the average fuel consumption across solutions obtained via the conditional global search approach is more uniformly distributed across the various scenarios. Conversely, the nonconditional global search approach exhibits significantly higher average fuel consumption for these scenarios, especially for the forward robust solutions.

C. Comparison of Solving Time

Table 8 Comparison of solving time per solution

		Non-Robust	Robust
Nonconditional Global Search	Total Time [h]	1,728	4,608
	Number of Solutions	687	1,465
	Time/Solution [h]	2.52	3.14
Conditional Global Search	Time/Solution [h]	2.52+0.33 = 2.85	

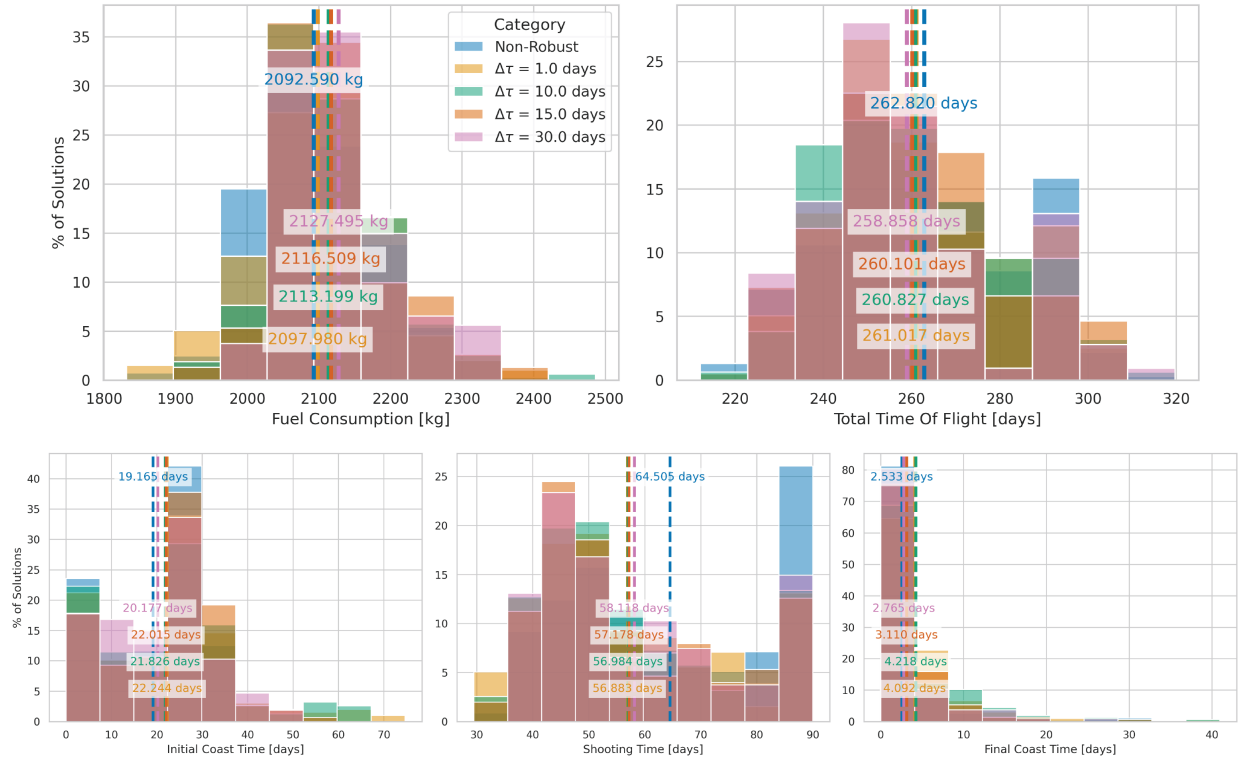


Fig. 10 Comparison of non-robust solutions with robust solutions via conditional global search categorized by $\Delta\tau$

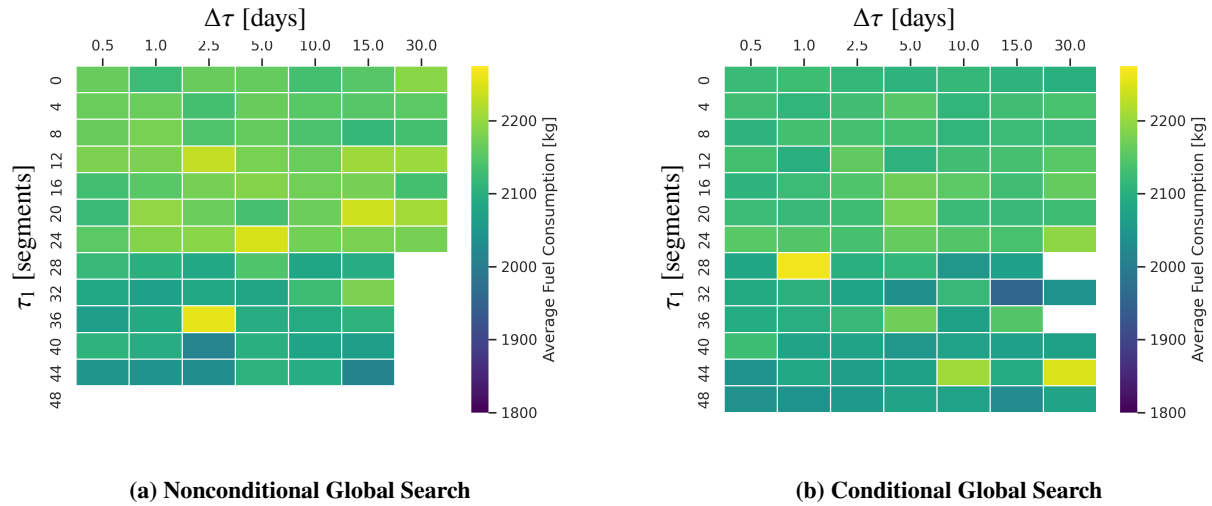


Fig. 11 Comparison of average fuel consumption for various τ_1 and $\Delta\tau$ using the nonconditional global search approach and the conditional global search approaches

By warm-starting the robust solutions with non-robust solutions, we not only improve the feasibility ratio and solution quality but also the convergence rates, as shown in Table 8. The solving time per solution for the robust case is 25% higher than that for the non-robust case when utilizing the nonconditional global search approach. This is in

line with our expectation, given that the robust case involves a higher-dimensional decision variable set, leading to a decrease in convergence rates. However, by using the robust solutions as initial guesses, we achieve a reduction in the time per solution by approximately 10% compared to the nonconditional global search approach. It is important to highlight that the time per solution for the robust case with the conditional global search approach comprises the average time per solution for the non-robust case using the nonconditional global search approach, in addition to the time required for the local solve process.

VII. Conclusion

This study presents a robust trajectory design framework applied to a high-fidelity low-thrust cislunar transfer for the Power and Propulsion Element (PPE). The proposed framework demonstrates several algorithmic improvements aimed at enhancing the efficiency of the global search for robust solutions. First, we introduce an adaptive segmentation strategy that ensures congruity in control authority between the reference and realization solutions. We present a comparative analysis between two global search strategies for robust solutions: a nonconditional search which involves a purely random sampling from an a-priori chosen bounded distribution and a conditional approach that leverages non-robust solutions as initial guesses for the robust solutions. Our results indicate that initializing the robust optimization process with non-robust solutions significantly enhances both convergence rates and solution quality. However, this approach also constrains the search within a basin of attraction where locally optimal robust solutions may not always exist, underscoring the trade-offs of warm-starting robust trajectories with non-robust solutions. The results in this paper are limited to a single missed thrust event with the reference solution being coupled with a single realization solution. Future work should expand the analysis to include scenarios where the reference solution is coupled with multiple realization solutions, and also scenarios with multiple missed thrust events, where the global search method may be more advantageous due to the increased number of realizations. Such extensions could provide deeper insights into the trade-offs in various global search strategies for robust low-thrust trajectory design in complex multibody dynamical environments.

Acknowledgments

The simulations presented in this article were performed on computational resources managed and supported by Princeton Research Computing, a consortium of groups including the Princeton Institute for Computational Science and Engineering (PICSciE) and the Office of Information Technology's High Performance Computing Center and Visualization Laboratory at Princeton University. The data that support this study are available from the authors upon reasonable request.

References

- [1] Imken, T., Randolph, T., DiNicola, M., and Nicholas, A., “Modeling spacecraft safe mode events,” *2018 IEEE Aerospace Conference*, Big Sky, MT, 2018.
- [2] McGuire, M., McCarty, S., Karn, S., Ponnappalli, K., Hack, K., Grebow, D., Pavlak, T., and Davis, D., “Overview of the Lunar Transfer Trajectory of the Co-manifested First Elements of NASA’s Gateway,” *AAS/AIAA Astrodynamics Specialist Conference*, Big Sky, MT (Virtual), 2021.
- [3] Whitley, R., and Martinez, R., “Options for Staging Orbits in Cis-Lunar Space,” *2015 IEEE Aerospace Conference*, Big Sky, MT, 2015.
- [4] Lee, D., “Gateway Destination Orbit Model: A Continuous 15 Year NRHO Reference Trajectory,” 2019.
- [5] McGuire, M. L., McCarty, S. L., and Burke, L. M., “Power and Propulsion Element (PPE) Spacecraft Reference Trajectory Document,” Tech. Rep. NASA/TM—2020-220481, March 2020.
- [6] Davis, D., Bhatt, S., Howell, K., Jang, J.-W. J., Whitley, R., Clark, F., Guzzetti, D., Zimovan, E., and Barton, G., “Orbit Maintenance and navigation of human spacecraft at cislunar Near Rectilinear Halo Orbits,” *AAS/AIAA Astrodynamics Specialist Conference*, San Antonio, TX, 2017.
- [7] Pritchett, R., Zimovan, E., and Howell, K., “Impulsive and low-thrust transfer design between stable and nearly-stable periodic orbits in the restricted problem,” *28th AIAA/AAS Space Flight Mechanics Meeting*, Kissimmee, FL, 2018.
- [8] Whitley, R. J., Davis, D. C., Burke, L. M., McCarthy, B. P., Rolfe, J. A., Power, M. L., and Howell, K. C., “Earth-Moon Near Rectilinear Halo and Butterfly Orbits for lunar surface exploration,” *AAS/AIAA Astrodynamics Specialist Conference*, Big Sky, MT, 2018.
- [9] McGuire, M., Burke, L., McCarty, S., Hack, K., Whitley, R., Davis, D., and Ocampo, C., “Low Thrust Cis-Lunar Transfers Using a 40 kW-Class Solar Electric Propulsion Spacecraft,” *AAS/AIAA Astrodynamics Specialist Conference*, San Antonio, TX, 2017.
- [10] Parker, J., “Low Energy Ballistic Lunar Transfers,” Ph.D. thesis, University of Colorado, Department of Aerospace Engineering Sciences, University of Colorado, 2007.
- [11] Parker, J., and Born, G., “Modeling a Low-Energy Ballistic Lunar Transfer Using Dynamical Systems Theory,” *Journal of Spacecraft and Rockets*, Vol. 45, No. 6, 2008, pp. 1269–1281. <https://doi.org/10.2514/1.35262>.
- [12] Parker, J., “Monthly Variations of Low-Energy Ballistic Transfers to Lunar Halo Orbits,” *AAS/AIAA Astrodynamics Specialist Conference*, Toronto, Canada, 2010.
- [13] Parker, J., Anderson, R., and Peterson, A., “A Survey of Ballistic Transfers to Low Lunar Orbit,” *21st AIAA/AAS Space Flight Mechanics Meeting*, New Orleans, LA, 2011.

- [14] Singh, S., Junkins, J., Anderson, B., and Taheri, E., “Eclipse-Conscious Transfer to Lunar Gateway Using Ephemeris-Driven Terminal Coast Arcs,” *Journal of Guidance, Control, and Dynamics*, Vol. 44, No. 11, 2021, pp. 1972–1988. <https://doi.org/10.2514/1.G005920>.
- [15] Pascarella, A., and Woollands, R., “Low Thrust Trajectory Optimization for Transporting Gateway’s Power and Propulsion Element to a Near-Rectilinear Halo Orbit,” *33rd Space Flight Mechanics Conference*, Austin, TX, 2023.
- [16] Singh, S. K., Anderson, B. D., Ehsan, T., and Junkins, J. L., “Low-Thrust Transfers to Southern L2 Near-Rectilinear Halo Orbits Facilitated by Invariant Manifolds,” *Journal of Optimization Theory and Applications*, Vol. 191, No. 2-3, 2021, pp. 517–544. <https://doi.org/10.1007/s10957-021-01898-9>.
- [17] Guzzetti, D., Zimovan, E., Howell, K., and Davis, D., “Stationkeeping Analysis for Spacecraft in Lunar Near Rectilinear Halo Orbits,” *27th AAS/AIAA Spaceflight Mechanics Meeting*, San Antonio, TX, 2017.
- [18] Capdevila, L., and Howell, K., “A Transfer Network Linking Earth, Moon, and the Triangular Libration Point Regions in the Earth-Moon System,” *Advances in Space Research*, Vol. 62, No. 7, 2018, pp. 1826–1852. <https://doi.org/10.1016/j.asr.2018.06.045>.
- [19] McCarty, S. L., and Grebow, D. J., “Missed Thrust Analysis and Design For Low Thrust Cislunar Transfers,” *AAS/AIAA Astrodynamics Specialist Conference*, South Lake Tahoe, CA, 2020.
- [20] Oshima, K., “The use of vertical instability of L1 and L2 planar Lyapunov orbits for transfers from near rectilinear halo orbits to planar distant retrograde orbits in the Earth-Moon system,” *Celestial Mechanics and Dynamical Astronomy*, Vol. 131, No. 3, 2019, p. 14. <https://doi.org/10.1007/s10569-019-9892-6>.
- [21] Zhang, R., Wang, Y., Zhang, H., and Zhang, C., “Transfers from distant retrograde orbits to low lunar orbits,” *Celestial Mechanics and Dynamical Astronomy*, Vol. 132, No. 8, 2020, p. 41. <https://doi.org/10.1007/s10569-020-09982-4>.
- [22] Trofimov, S., Shirobokov, M., Tselousova, A., and Ovchinnikov, M., “Transfers from near-rectilinear halo orbits to low-perilune orbits and the Moon’s surface,” *Acta Astronautica*, Vol. 167, 2020, pp. 260–271. <https://doi.org/10.1016/j.actaastro.2019.10.049>.
- [23] Rayman, M. D., Frascetti, T. C., Raymond, C. A., and Russell, C. T., “Coupling of System Resource Margins through the Use of Electric Propulsion: Implications in Preparing for the Dawn Mission to Ceres and Vesta,” *Acta Astronautica*, Vol. 60, No. 10, 2007, pp. 930–938. <https://doi.org/10.1016/j.actaastro.2006.11.012>.
- [24] Oh, D., Landau, D., Randolph, T., Timmerman, P., Chase, J., Sims, J., and Kowalkowski, T., “Analysis of System Margins on Deep Space Missions Using Solar Electric Propulsion,” *44th AIAA/ASME/SAE/ASEE Joint Propulsion Conference & Exhibit*, 2008. <https://doi.org/10.2514/6.2008-5286>.
- [25] Laipert, F. E., and Longuski, J. M., “Automated Missed-Thrust Propellant Margin Analysis for Low-Thrust Trajectories,” *Journal of Spacecraft and Rockets*, Vol. 52, No. 4, 2015, pp. 1135–1143. <https://doi.org/10.2514/1.A33264>.
- [26] Laipert, F. E., and Imken, T., “A Monte Carlo Approach to Measuring Trajectory Performance Subject to Missed Thrust,” *28th AIAA/AAS Space Flight Mechanics Meeting*, Kissimmee, FL, 2018. <https://doi.org/10.2514/6.2018-0966>.

- [27] Sinha, A., and Beeson, R., “Recovery From Missed Thrust During Low Thrust Insertion Of NASA’s Gateway Into A Near Rectilinear Halo Orbit,” *AAS/AIAA Astrodynamics Specialist Conference*, Broomfield, CO, 2024.
- [28] Venigalla, C., Englander, J. A., and Scheeres, D. J., “Multi-Objective Low-Thrust Trajectory Optimization with Robustness to Missed Thrust Events,” *Journal of Guidance, Control, and Dynamics*, Vol. 45, No. 7, 2020, pp. 1255–1268. <https://doi.org/10.2514/1.G006056>.
- [29] Sinha, A., and Beeson, R., “Statistical Analysis of the Role of Invariant Manifolds in Robust Low-Thrust Trajectory Design in Multibody Dynamical Systems,” *Journal of Guidance, Control, and Dynamics (not yet published)*, 2024.
- [30] Beeson, R., Sinha, A., Jagannatha, B., Bunce, D., and Carroll, D., “Dynamically Leveraged Automated (N) Multibody Trajectory Optimization (DyLAN),” *AAS/AIAA Astrodynamics Specialist Conference*, Columbia River Gorge, Stevenson, WA, 2022.
- [31] Betts, J. T., “Survey of Numerical Methods for Trajectory Optimization,” *Journal of Guidance, Control, and Dynamics*, Vol. 21, No. 2, 1998, pp. 193–207. <https://doi.org/10.2514/2.4231>.
- [32] Gill, P. E., Murray, W., and Saunders, M. A., “SNOPT: An SQP Algorithm for Large-Scale Constrained Optimization,” *SIAM Review*, Vol. 47, No. 1, 2005, pp. 99–131.
- [33] Wales, D. J., and Doye, J. P., “Global optimization by basin-hopping and the lowest energy structures of Lennard-Jones clusters containing up to 110 atoms,” *The Journal of Physical Chemistry A*, Vol. 101, No. 28, 1997, pp. 5111–5116.
- [34] Leary, R. H., “Global optimization on funneling landscapes,” *Journal of Global Optimization*, Vol. 18, No. 4, 2000, p. 367.
- [35] Englander, J., Conway, B., and Williams, T., “Automated Interplanetary Mission Planning,” *AAS/AIAA Astrodynamics Specialist Conference*, 2012. <https://doi.org/10.2514/5.9781624102714.0669.0706>.
- [36] Englander, J. A., and Englander, A. C., “Tuning monotonic basin hopping: improving the efficiency of stochastic search as applied to low-thrust trajectory optimization,” *International Symposium on Space Flight Dynamics*, Laurel, MD, 2014.
- [37] Englander, J. A., and Conway, B. A., “Automated solution of the low-thrust interplanetary trajectory problem,” *Journal of Guidance, Control, and Dynamics*, Vol. 40, No. 1, 2017, pp. 15–27. <https://doi.org/10.2514/1.G002124>.
- [38] Sinha, A., and Beeson, R., “Accelerating Robust Low-Thrust Trajectory Design with Analytic Derivatives,” *AAS/AIAA Astrodynamics Specialist Conference*, Kauai, HI, 2025.
- [39] Acton, C. H., “Ancillary data services of NASA’s Navigation and Ancillary Information Facility,” *Planetary and Space Science*, Vol. 44, No. 1, 1996, pp. 65–70. [https://doi.org/10.1016/0032-0633\(95\)00107-7](https://doi.org/10.1016/0032-0633(95)00107-7).